Title

Detection and Analysis of Aleutian Arc Seismicity (2022—2023) Using an Autonomous Hydrophone Array

Journal

Geochemistry Geophysics Geosystems, 26(8)

ISSN

1525-2027

Authors

Ingale, Vaibhav Vijay

Tepp, Gabrielle

Dziak, Robert P

et al.

Publication Date

2025-08-01

DOI

10.1029/2025gc012320

Detection and Analysis of Aleutian Arc Seismicity (2022-2023) Using an Autonomous Hydrophone Array

Vaibhav Vijay Ingale[1], Gabrielle Tepp[2], Robert P Dziak[3], Ross Parnell-Turner[1]

[1]Institute of Geophysics and Planetary Physics, Scripps Institution of Oceanography, University of California San Diego, La Jolla, CA, USA

[2]Seismological Laboratory, Caltech, Pasadena, CA, USA

[3]Pacific Marine Environmental Laboratory, National Oceanic and Atmospheric Administration, Newport, OR, USA

Corresponding author: Vaibhav Vijay Ingale (vingale@ucsd.edu)

Key Points:

- Hydroacoustic detections in 2022-2023 along the Aleutian Arc using an array of four hydrophones moored in the Bering Sea
- Two main types of signals observed, long duration (~40 s) T-phases and short duration (~10 s) impulsive signals
- Short-duration impulsive signals are attributed to seismic unrest beneath Tanaga Island and likely caused by shallow magma transport

Abstract

The Aleutian trench, extending from the Gulf of Alaska to Kamchatka, marks the subduction boundary between the Pacific and North-American plates. It hosts the Aleutian Islands, one of Earth's most significant volcanic arcs, with 52 historically active volcanoes. Given the long history of eruptions and strong earthquake-induced tsunamis that pose hazards to Aleutian communities, studying this area is essential for assessing geohazards and subduction zone processes. To investigate submarine volcanism and seismicity along the western Aleutian Islands, four autonomous underwater hydrophones (AUH) were deployed in June 2022 for 12 months ~100 km north of Adak Island. The AUHs were moored at depth of ~500 m in a diamond-shaped array with 10 km spacing. The AUHs recorded different types of acoustic signal packets (events), including, long-duration (~40s) spindle-shaped T-phases with frequencies <60 Hz; that are characteristics of tectonic earthquakes and short-duration (~10s), impulsive signals with a wide range of frequencies (40-100 Hz) were observed, peaking in activity during March 2023; that are associated with shallow seismic events. We characterized all hydroacoustic events by their temporal distribution, back-azimuths, rise time, and received level, to establish acoustic signal categories based on the likely source mechanisms. By comparing hydroacoustic detections with a land-based earthquake catalog, we observe that short-duration events originated from seismic unrest beneath Tanaga Island. The temporal distribution of magnitudes and depths of seismic events, coupled with rise times and received levels of matched hydroacoustic signals, suggests that the seismic unrest is linked to magma transport at shallow depths beneath Tanaga Island.

Plain Language Summary

The Aleutian Island arc, formed by the convergence of two tectonic plates in the north Pacific, hosts several active volcanoes. These volcanic centers produce seismicity through mechanisms such as subsurface magma movement, volcanic eruption, and subduction processes. But seismic monitoring is difficult due to their remoteness and the limited availability of land-based stations. We analyze a year-long hydroacoustic data recorded on an array of four hydrophones moored in the Bering Sea. We detected 4,586 hydroacoustic events mainly consisting of two types: long

duration (~40 s) T-phases and short-duration (~10 s) impulsive signals. These events were characterized by temporal distribution, source direction, wave shape, and acoustic energy. After correlating these events with the records from the United States Geological Survey earthquake catalog, we observed that the impulsive signals are primarily associated with the seismic unrest beneath the Tanaga volcanic center, situated in the central western part of the volcanic arc. We observed distinct periods of higher seismic activity, both in the hydroacoustic and seismic catalogs, which we attribute to subsurface magmatic processes occurring during the Tanaga unrest between November 2022 and March 2023.

1 Introduction

The Aleutian Arc in the north Pacific Ocean is a prominent volcanic island-arc extending over 3,000 kilometers from the Gulf of Alaska to Kamchatka (Figure 1). This arc is formed by the subduction of the Pacific plate beneath the North American plate at a rate of 6.6 to 8.6 cm/yr (Lallemant, 1996). This subduction zone is expressed at the seabed as the Aleutian Trench, creating a highly active tectonic environment characterized by seismic and volcanic activity (e.g., Benz et al., 2010; Buurman et al., 2014). The complex interaction between these tectonic plates has generated a series of 52 historically active volcanic centers along the arc, making the region one of the Earth's most active volcanic zones with substantial potential for geohazards, particularly for commercial air traffic (e.g., Murray et al., 2009; Herrick et al., 2014; Larsen, 2016; Wang et al., 2023).

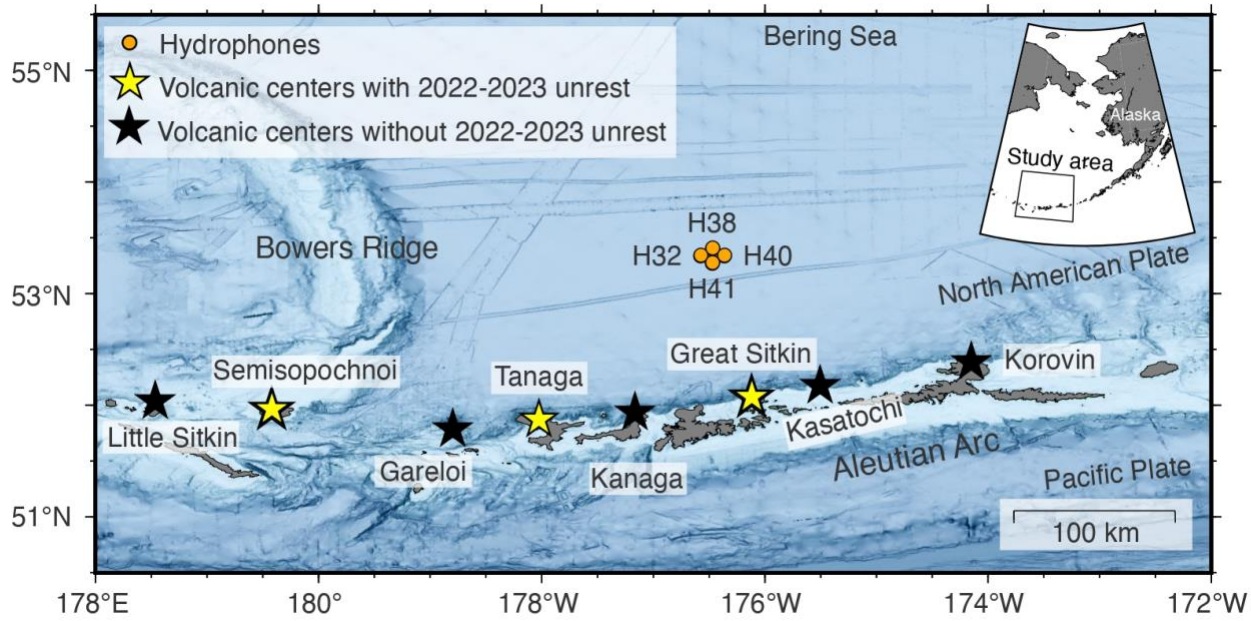

Figure 1: Locations of four hydrophones (orange circles) deployed by PMEL-NOAA in the Bering Sea, north of the Aleutian arc in 2022-2023. Yellow stars show volcanic centers that experienced unrest and eruption in 2022-2023 (Global Volcanism Program, 2023a, 2023b, 2023c). Black stars show volcanic centers that did not experience unrest. Bathymetry is from Ryan et al. (2009).

In the central-western portion of the Aleutians, Tanaga and other neighboring volcanic centers including Great Sitkin and Semisopochnoi have experienced periodic seismic unrest, which can signal impending volcanic eruptions or regional tectonic deformation (Cameron et al., 2023; Orr et al., 2024a, 2024b). Tanaga experienced three non-eruptive episodes between 2005 and 2023, occurring at ~9-year intervals, with recent seismic unrest in 2023, although its last eruption was in 1914. Great Sitkin has experienced nine documented eruptive episodes (in 1933, 1945, 1949, 1950, 1974, 2018, 2019, 2021-2025), and five documented non-eruptive episodes (in 1953, 2001, 2002, 2013, and 2020). Semisopochnoi has undergone six eruptive episodes (1873, 1987, 2018, 2019, 2020 and 2021-2023) and two non-eruptive episodes (2014 and 2015; Coombs et al., 2018; Cameron et al., 2023).

Seismicity in such arc volcanic islands can result from diverse seismogenic source mechanisms, such as magma upwelling (Yang and Gao, 2020), active volcanic unrest or eruptions (Tepp et al.,

2020), thrust faulting from the subducting Pacific plate (Jiang et al., 2022), or the deformation of the overriding crust (Janiszewski et al., 2013). Monitoring this seismicity is essential to understand active magmatic systems and the dynamics of eruptions, and to assess associated hazards. However, seismic monitoring in island arcs faces significant difficulties due to their remoteness, rugged terrain, and challenges of maintaining land-based seismic stations. The sparse network of stations, particularly in the central and western parts of the arc, leads to gaps in network coverage, reducing the accuracy of detecting and locating seismic events (Li, 2021).

Autonomous underwater hydrophones offer a complementary monitoring approach by detecting underwater acoustic signals generated by seismic activity (e.g., Fox et al., 2001). These hydrophones are sensitive to low-frequency acoustic waves (typically down to 1 Hz), resulting from seismic-to-acoustic conversion at the seafloor, enhancing the detection of submarine earthquakes and volcanic eruptions (e.g., Tepp and Dziak, 2021). By integrating hydrophone networks with seismic networks, such as those operated by the Alaska Earthquake Center and Alaska Volcano Observatory (Figure S1), it becomes possible to monitor seismic activity more effectively in remote island arcs, improving our understanding of seismic hazards in these regions (Tepp, 2024).

Between June 2022 and June 2023, the Pacific Marine Environmental Laboratory of the National Oceanic and Atmospheric Administration (PMEL-NOAA) deployed a network of four hydrophones ~100 km north of Adak Island (Dziak et al., 2023) to record a baseline of hydroacoustic signals from geophysical activity and to survey for possible submarine volcanism, which has been poorly studied in the Aleutian Arc. Because much of the arc is geographically remote, regional seismic networks maintained by the Alaska Volcano Observatory and Alaska Earthquake Center provide limited coverage, and as a result, many smaller or offshore events may go undetected or remain poorly characterized. To address these limitations, this study uses the hydroacoustic data to detect and characterize seismic activity, and its relation with tectonic or volcanic sources. First, we manually detect acoustic events, classify them into different types based on signal duration and frequency content. We then characterize them in terms of their back-azimuths, rise times, and received levels. Finally, we correlate hydroacoustic signals with the United States Geological

Survey (USGS) earthquake catalog, to obtain the acoustic baseline for the trench and Aleutian Arc volcanoes which experienced unrest or volcanic eruptions in 2022-2023.

2 Materials and Methods

2.1 Hydroacoustic detections

We analyzed data recorded by four hydrophones moored at 500 m depth below the sea surface, suspended in the water column and anchored by cables to the seafloor (Table S1). The mooring line consists of a disposable anchor on the seafloor, an acoustic release, adjustable-length cables positioning the hydrophone in the Sound Fixing and Ranging channel, and a float that keeps the line taut, protects the recorded housed in a titanium cylinder during acquisition (Haxel et al., 2013). They are arranged in a diamond-shaped geometry with 10 km spacing (Table S1, Figure 1). All the hydrophones were operational from 16 June 2022 to 22 June 2023 and recorded acoustic waves continuously at a sampling rate of 2,000 Hz in 16-bit samples. The collected data were analyzed with software developed at PMEL-NOAA in IDL (Interactive Data Language Research Systems, Boulder, Co.; Fox et al., 2001). Each event was located after manually picking the highest signal energy in spectrograms. Once signals were identified on at least three hydrophones, the origin time in UTC and source location were estimated using a non-linear least-squares minimization of the arrival times of peak energy (Fox et al., 2001). Sound velocities in the ocean were based on the three-dimensional and seasonal Global Digital Environment Model at a resolution of 30 arc-minutes in latitude and longitude (Teague et al., 1990). For our use, an accurate source location estimation depends on absolute travel times over longer distances, which could be more sensitive to spatial variations in ocean sound velocity profile. But due to the small aperture and distance of the hydrophone array, resulting locations have high uncertainty, so we do not consider this method of source locations further (Figure S2).

2.2 Back-azimuth of events

We computed the back-azimuth for each event based on the arrival time of peak energy. We converted arrival times into distance differences by multiplying by the water velocity of 1.462

km/s. The hydroacoustic sound speed profile in the region is a polar half-channel (e.g., Kutschale 1969) with a near-surface (~200 m depth) low-velocity layer (surface duct). We computed the water velocity using average temperature and salinity data obtained from a hindcast of the World Ocean Atlas (Reagan et al., 2024) along a great circle path between the hydrophones and Tanaga Island, sampled at 10 km intervals at a depth of 200 m. This velocity model is suitable for azimuth estimation because it relies on relative arrival-time difference across a hydrophone array geometry rather than absolute travel times. Using the hydrophone locations and the calculated distance differences, we formulated an objective function *f(x,y)* of hyperbolic form,

$$f(x,y) = \sum_{i,j=1}^{4} \left(\sqrt{(x-x_a)^2 + (y-y_a)^2} - \sqrt{(x-x_b)^2 + (y-y_b)^2} - \Delta d_{ab} \right)^2$$

where (x, y) is an intersection point with x as longitude and y as latitude, (x_a, y_a) and (x_b, y_b) are the coordinates of the hydrophones and Δd_{ab} is the distance difference calculated from relative arrival times on each pair of hydrophones a, b, multiplied by velocity. By minimizing this objective function for each pair of hydrophones, we identified a common intersection point of the hyperbolic equations and estimated event back-azimuth, calculated as the clockwise angle from geographic north to the line connecting the mean location of the hydrophone network to the intersection point. In the south Bering sea (51°N-55°N), the standard deviation in sound velocity at 200 m was ± 3 m/s, indicating a relatively stable environment at different locations. For the least-squares minimization, this small variation in velocity accounts for uncertainty of 0.5-0.8° in back-azimuth estimation.

2.3 Event Received Level

Hydroacoustic events can be characterized by the acoustic magnitude or acoustic source level, which are derived from the received levels (RL) at each hydrophone and corrected for the transmission loss between the event and the hydrophone locations (Williams et al., 2006; Royer et al., 2015). The TL accounts for the cylindrical sound-spreading loss between the event location and the hydrophone, as well as the spherical sound-spreading loss in the water column between the seafloor acoustic radiator and the sound channel axis (e.g., Jensen et al., 1994; Dziak, 2001).

As estimating the precise source location is not possible for our events, TL computation is not reliable, and hence source level would not be an accurate representation of acoustic magnitude for each event. Instead, the RL expressed in decibels with respect to 1 micro-Pascal at 1 meter (hereinafter dB) can serve as a relative measure to compare the acoustic strength of detected events, although it does not correlate directly with earthquake magnitude. This parameter is based on the average power spectral density in a 10-second window centered on the peak of energy in the acoustic signal on each hydrophone.

2.4 Earthquake catalog

Between June 2022 and June 2023, the USGS earthquake catalog contained 14,059 events along the Aleutian arc (region of Figure 1), with 5,946 of these occurring near Tanaga Island (Alaska Earthquake Center, 1987; Alaska Volcano Observatory, 1988; Albuquerque Seismological Laboratory, 1990). The greatest event density (per km²) was observed between the Tanaga and Takawangha volcanic centers (Figure 2a). These events were mainly concentrated in three seismic unrest episodes: 268 events from 18-20 November 2020, 281 events from 17-20 February 2023, and 2,849 events from 8-15 March 2023 (Figure 2b). Across all episodes, local magnitudes (M_L) ranged from 0.0 to 4.4 (Figure 2c). In all the three episodes, earthquakes were located at depths of less than 10 km (Figure 2d, S7). Despite the intense seismic activity, these episodes did not lead to volcanic eruption (Global Volcanism Program, 2023a).

In contrast, Great Sitkin began an eruption in 2021 which subsided during January-April 2022 but continued until April 2023 with slow lava effusion accompanied by steam-and-gas-emissions and very mild seismicity (Global Volcanism Program, 2023b). Between June 2022 and June 2023, the USGS catalog contained only 179 events near Great Sitkin. Similarly, Semisopochnoi Island had several intermittent eruptive episodes between 27 December 2022 and 25 April 2023, accompanied by seismic tremors, gas-and-steam plumes, small explosions, and infrequent seismic activity (Global Volcanism Program, 2023c).

In this study, we identified ‘matched’ events that are common in both the seismic and hydroacoustic catalog by comparing their origin time and back-azimuths. We initially estimated

191 the approximate acoustic travel time from the seismic event locations to hydrophone H41, using
192 the water speed of 1.462 km/s. This estimated travel time was then compared to the observed
193 arrival time of peak energy at the hydrophone. A match was considered valid when the time
194 difference was within ± 20 s, as more than > 95% of hydroacoustic phases were clearly detectable
195 within this time window. This threshold was determined empirically during the catalog
196 development process. We found that more than 95% of individual hydroacoustic phases were
197 separated by at least 20 seconds, minimizing phase overlap and allowing for reliable
198 identification and association with corresponding seismic events. A histogram measuring the
199 difference between observed and estimated arrival time is shown in Figure S3. Additionally, for
200 the matched events, we computed the back-azimuths relative to H41 hydrophone and further
201 refined the catalog of matched events by only retaining events when the azimuths were within
202 limits of ± 10° with respect to azimuths of hydroacoustic signals, when measured from
203 hydrophone array. Out of 4,586 hydroacoustic signals, we found seismic matches for 3,174
204 events (69%). In the subsequent sections, we will discuss their spatial distribution.

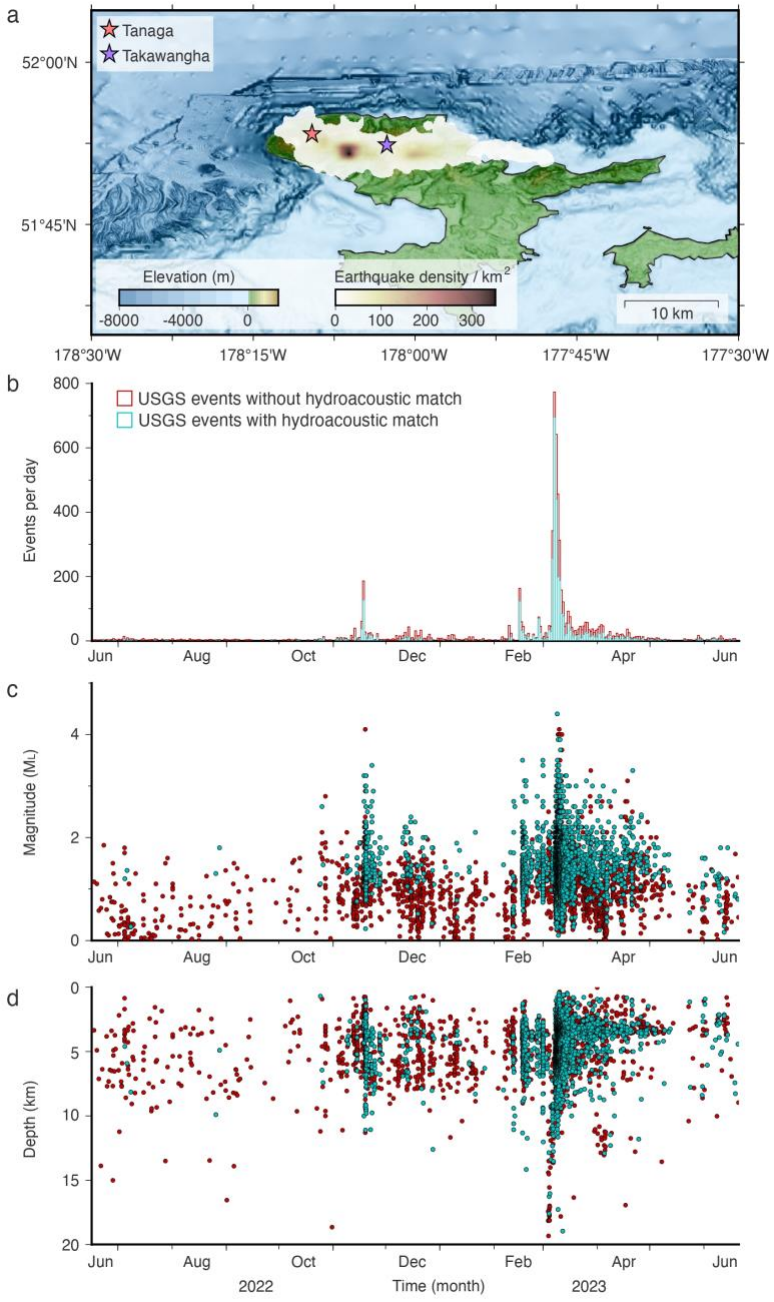

Figure 2: a) Earthquake density per km^2 between 16 June 2022 and 22 June 2023 on Tanaga Island obtained from USGS catalog (Alaska Earthquake Center, 1987; Alaska Volcano Observatory, 1988; Albuquerque Seismological Laboratory, 1990); relief is from Ryan et al. (2009). **b)** Histogram of number of events per day and the temporal distribution of **c)** local magnitudes and **d)** depths. Red histogram/dots show all the USGS events near Tanaga Island in 2022-2023 and blue histogram/dots show only USGS events with a hydroacoustic match.

3 Results and Interpretation

3.1 Detection of contrasting types of acoustic signals

In our hydroacoustic analysis, we detected 4,586 events and classified them into two main categories based upon their time and frequency domain character: T-phases and short-duration impulsive events (Figure 3). This classification may help to provide a comprehensive framework for understanding the diversity of signals in volcanic island arc settings, particularly in the context of the central and western Aleutian Arc, which has not been extensively characterized with long-term hydroacoustic monitoring.

In the first category, the spindle-shaped waveforms are characterized by a gradual amplitude increase, a peak at frequencies up to 60 Hz, and a trailing coda wave signal (Figure 3a-b). They are called T-phases (tertiary) as they travel at water velocity and arrive after P and S phases. We further classified T-phases into four different types. First signals are those where T-phases were detected without preceding P and S phases. Second, here termed composite PST-phases, are T-phases for which the faster arriving P and S waves were also detected (Figure 3c-d). Although hydrophones are optimized for acoustic wave detection, earthquake P and S arrivals waves are still detectable as hydroacoustic waves converted at the seafloor near the mooring or by induced motion of the hydrophone mooring (e.g., Dziak et al., 2004a). The mean time difference between P and S phases for all the composite PST events was ~25 s, S and T was ~70 s, and P and T was ~95 s (Figure S4). We used these time differences to estimate the source to array distance by accounting the P-wave, S-wave and T-wave velocities of 8 km/s, 4.6km/s and 1.462 km/s, respectively. The S-P time difference yields a distance of ~260 km, whereas P-T and S-T time difference yield a distance of ~170 km and ~150 km, respectively. The distance between the hydrophone array and Aleutian Arc trench ranges from 140-220 km, which is consistent with the distances computed using P-wave, S-wave and T-wave time differences. The third type, here named composite PT-phases, are T-phases that appear immediately following P-wave arrivals without detectable S arrivals (Figure 3e-f). Lastly, paired T-phases appear sequentially after the P and S arrivals (Figure 3g-h). Similar to PST events, these paired events have P-S time difference of 22-29 s and S-T time difference of 70-75 s. The time interval between the peak amplitudes of

these paired T-phases ranges from 10 to 120 seconds (Figure S4). These paired signals have nearly identical spectral characteristics suggesting a common source, but the temporal separation between them implies different excitation mechanisms, such as multiple acoustic propagation paths or secondary conversions at separate bathymetric features, or closely spaced repeated source emissions. This repeated acoustic pattern in paired T-phases suggests complex propagation or source processes not observed in typical PST events. All T-phases in these categories exhibit total signal durations up to 40 seconds.

The second category of signals consisted of short-duration (~10 s) phases with frequencies in the range of 40-100 Hz, and we further classified them into four types. First, we detected phases lasting approximately 8 s with frequencies up to 70 Hz and called them impulsive I phases (Figure 3i-j). The second type, termed impulsive II phases, exhibited frequencies reaching up to 100 Hz in the first signal and multiple smaller phases up to 50 Hz, with an average interval of approximately 55 seconds between the initial and the first subsequent phase of the impulsive II events (Figures 3k-l, S5). While the spectral differences between impulsive I and II subtle, impulsive II exhibited secondary arrivals suggestive of either complex path processes or multiple closely time events. It is possible that these represent the same general event type but occur at different depths or in varying source environments, leading to the observed variability. The third type of signals consisted of two closely spaced short-duration phases with frequencies up to 50 Hz, and we called them doublets. (Figures 3m-n). The time difference between individual phases ranged from 2 to 120 s with a mean of ~32 s for all the doublet events (Figure S5). The occurrence of closely spaced phases in both impulsive II and doublet signals could be associated with reflections from different acoustic radiators or multiple conversion points. For example, Tepp et al. (2020) also noted reflected signals spaced ~2 min apart with highly similar characteristics from seismicity associated with the Bogoslof eruption in 2016-17. Given the variable time differences between two doublet phases and their highly spectral content, however, it is also plausible that these signals represent two distinct seismic events occurring in close temporal proximity. These signals may arise from repeated ruptures at the same source or near-simultaneous activity from adjacent sources. To evaluate this possibility, we cross-matched the doublet events with the USGS earthquake catalog. In nearly all cases, only one of the two pulses in a doublet matched a

cataloged seismic event. We then spot-checked a few of the doublets on Tanaga Island seismic station (AV.TANO) and found signals from events that were not cataloged, further supporting the possibility. While we cannot definitively rule out complex reflection or scattering effects along the Aleutian Arc geometry, the possibility of temporally clustered, spectrally similar events is a likely alternative explanation that fits both the observed time delays and spectral similarities. Lastly, the signals of generally low amplitude, with poorly defined durations and frequencies reaching up to 40 Hz, were classified as an uncategorized group (Figure 3o-p). These events may represent low-SNR variants of the other impulsive type, particularly impulsive I events, though their weak characteristics preclude confident classification into that category.

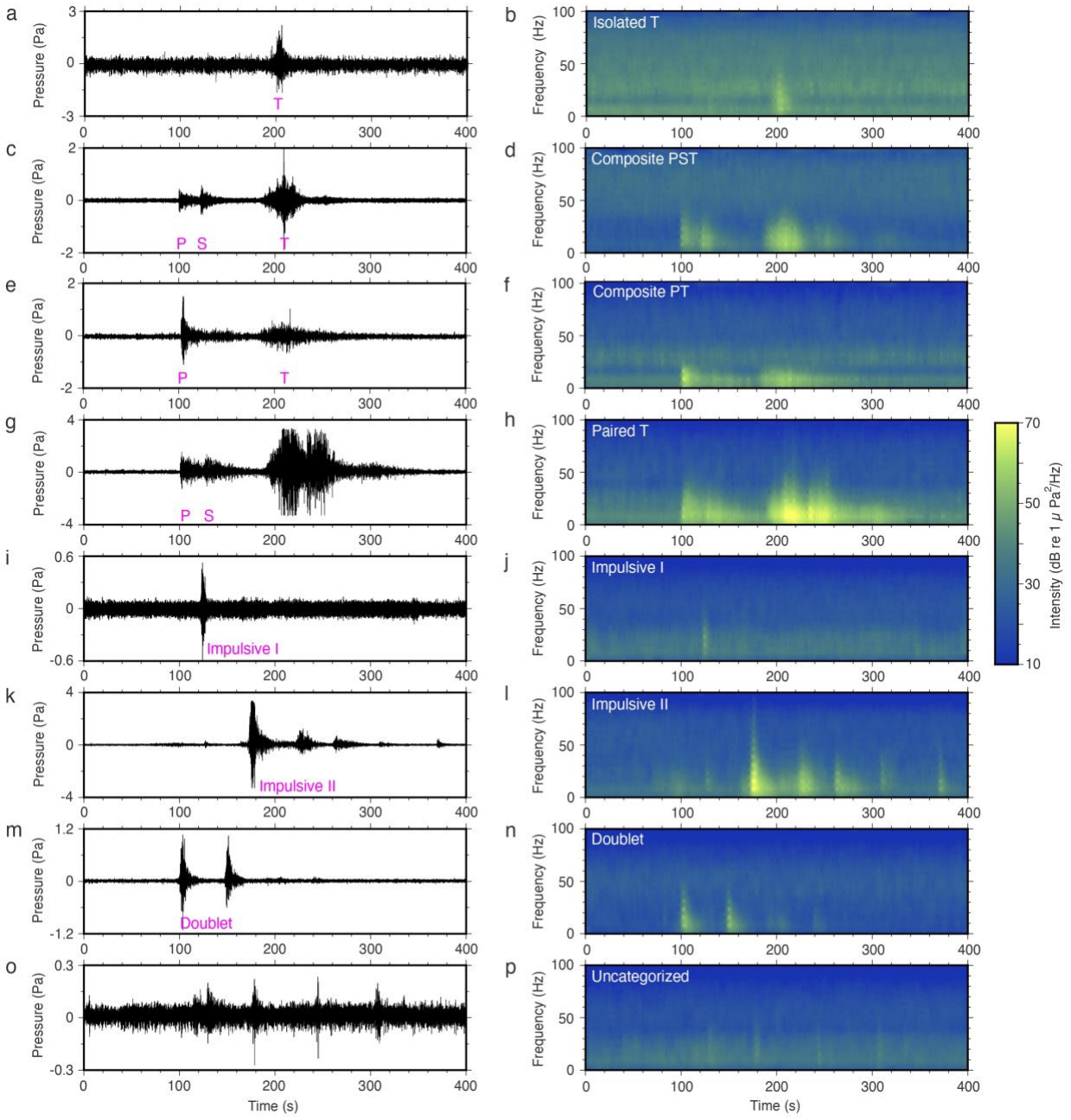

278

279 **Figure 3**: Waveforms and spectrograms of representative signals: **a-b)** spindle-shaped isolated T-
280 phase, **c-d)** composite PST phase, **e-f)** composite PT phase, **g-h)** paired T-phase after P and S, **i-j)**
281 impulsive I phase, **k-l)** impulsive II phase followed by weak amplitude phases, **m-n)** doublet
282 phase, and **o-p)** uncategorized phase having weak amplitudes and frequencies; waveforms are
283 shown unfiltered.

The reduced spectral frequency up to 40 Hz observed in the secondary signals of the impulsive II phase (Figure 3l), compared to paired T (Figure 3h) or doublet phases (Figure 3n), could result from differences in the coupling mechanisms of seismic energy into the water and the propagation characteristics of the signals. One possibility is that the differences in the geometry or depth of the secondary source may lead to less efficient transmission of seismic energy into the water column. Propagation effects such as increased acoustic absorption, scattering, or longer and more complex travel paths may further reduce the frequency content recorded at the hydrophone. The origin or path of the secondary phase of the paired T or doublet signal may be more optimally positioned or oriented to transmit acoustic energy efficiently, leading to overall frequency similar to the primary one. The paired T or doublet phases may follow more direct propagation paths with lower energy loss, whereas impulsive II phases might involve more complex propagation routes, leading to greater dissipation or interference and resulting in a decrease in observed energy in the secondary phases.

3.2 Power spectral density

To understand the frequency content of each type of signal in detail, we computed the mean power spectral density (PSD) for a sample of 20 events chosen at random from each of the eight signal types (Figure 4). For the analysis, the first three T-phase types were grouped into a combined T-phase category as they showed similar PSDs, amounting to 60 randomly selected events. Across all signal categories, the PSD exhibited significantly higher power at frequencies below 20 Hz. The paired T-phases displayed the highest PSD below 15 Hz, highlighting the strong low-frequency content in these signals. At higher frequencies, however, this power was exceeded by the impulsive II phases, which maintain high PSD values across a wider frequency range. The combined T-phase category exhibited a PSD profile falling below that of paired T and impulsive II phases. Impulsive I phases showed a PSD curve that aligns closely with that of doublet phases up to approximately 20 Hz, suggesting similar spectral characteristics in this frequency range. Above 20 Hz, doublet phases showed slightly higher PSD than impulsive I phases. The uncategorized signals exhibited the lowest PSD overall, deviating markedly from the other signal types.

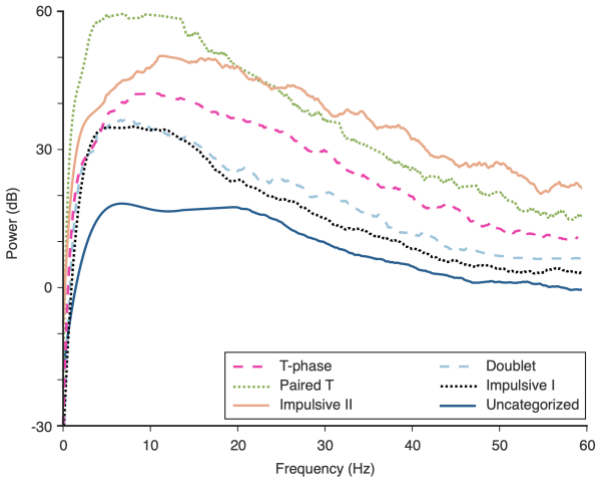

Figure 4: Average power spectral density of randomly selected events for different types of signals: T-phases, impulsive I, impulsive II, doublet, and uncategorized phases.

The elevated PSD values of paired T-phase and impulsive II signal types over a broad frequency range indicates efficient coupling of seismic energy into the water, with minimal attenuation and preserved signal strength across frequencies, facilitating effective propagation through the ocean. This efficiency may be driven by multiple factors, including favorable source-receiver geometries and signals originating from ideal spatial locations, likely associated with multiple acoustic conversion points or closely situated acoustic radiators that also generate secondary signals (Figure 3g, 3k). The PSD similarities between hydroacoustic signal types may also provide a basis for future classification and clustering efforts, allowing for improved automated identification of hydroacoustic signals in marine monitoring networks.

3.3 Spatio-temporal distribution of events

All the detected hydroacoustic phases showed large variability in their spatial and temporal distributions (Figures 5 and 6). While the geometry of a small aperture hydrophone array makes it difficult to precisely locate events, it can be used to calculate back-azimuths to the source. In island arcs and subduction zone settings, a back-azimuth from a well-placed array is generally sufficient to determine the source when considering the geologic features of the region.

The isolated T-phases exhibited a gradual increase in occurrence rate throughout hydrophone deployment except for a notable increase during 18-21 November, which coincided with the first period of Tanaga unrest (Figure 5). Following this time, isolated T-phase occurrence was relatively low until March 2023. From April 2023 to the end of deployment, the activity rate again showed gradual increase. T-phase back-azimuth distribution appeared mostly random across a wide range of directions. However, 68 events between 18-21 November 2022 showed a consistent back-azimuth towards Tanaga, confined within a ±10° range from its azimuth relative to the hydrophones. Out of 68 isolated T-phase events, we identified the matched seismic events for 56 (Table S2 and Figure S6a). The locations of matched events are widespread on the island, suggesting that the island geometry does not appear to systematically favor or impede acoustic energy generation. The remaining three T-phase categories (composite PST, PT, and paired T) did not display any clear temporal patterns or changes in activity rate. These three categories primarily had southeastern back-azimuths, oriented towards Great Sitkin and further east. None of these T-phases (composite PST, PT, and paired T) show a spatio-temporal pattern that is consistent with the Tanaga unrest. We compared them with the USGS catalog events along Great Sitkin between June 2022 and June 2023, but only 44 hydroacoustic matched events were found, which were arbitrarily distributed in time and along island without any clustering. Aside from the brief episode of potential association with Tanaga in November 2022, the main set of T-phases (516 out of 628) did not exhibit spatio-temporal patterns consistent with activity related to any of the volcanic islands (Tanaga, Great Sitkin or Semisopochnoi), we do not interpret them further, in the context of either unrest (near Tanaga) or eruption (near Great Sitkin and Semisopochnoi).

The remaining four categories of acoustic phases (impulsive I, II, doublet and uncategorized) peaked during Tanaga seismic unrest periods (Figure 6). Impulsive I events were observed during all three periods of Tanaga unrest, i.e., 18-21 November 2022 and 8-12 February and 8-15 March 2023, whereas impulsive II events only initiated during the March unrest, with a gradual decrease in the following weeks. Doublets were less frequent, with sporadic activity seen only in the March unrest, and similar observations were made for uncategorized events. In terms of spatial distribution, 1,268 out of 2,110 impulsive I events (60%) had back-azimuths consistently toward Tanaga Island. This alignment was prominent during all three periods of Tanaga unrest. Similarly,

137 of the 225 impulsive II events (60%), 41 out of 69 doublet events (59%), and 563 out of 1,554 uncategorized events (36%) also aligned with Tanaga's azimuth, consistent with intense seismic activity localized around this region. This spatio-temporal distribution confirms that the short-duration signals are associated with the Tanaga seismic unrest. For each type of short-duration signal, we identified the matched seismic events (Table S2), and their spatial distribution is shown in Figure S6b-e. All matched events are widely located across the island, similar to isolated T-phases.

While many of the uncategorized events appear to have back-azimuths pointing between Tanaga and Kanaga Islands (Figure 6h), notably we did not find consistent seismic matches corresponding to sources located between these islands during the study period (2022-2023). This apparent clustering may be influenced by acoustic propagation effects or possibly undocumented seismic activity in this region or due to larger uncertainty in the back-azimuth estimation.

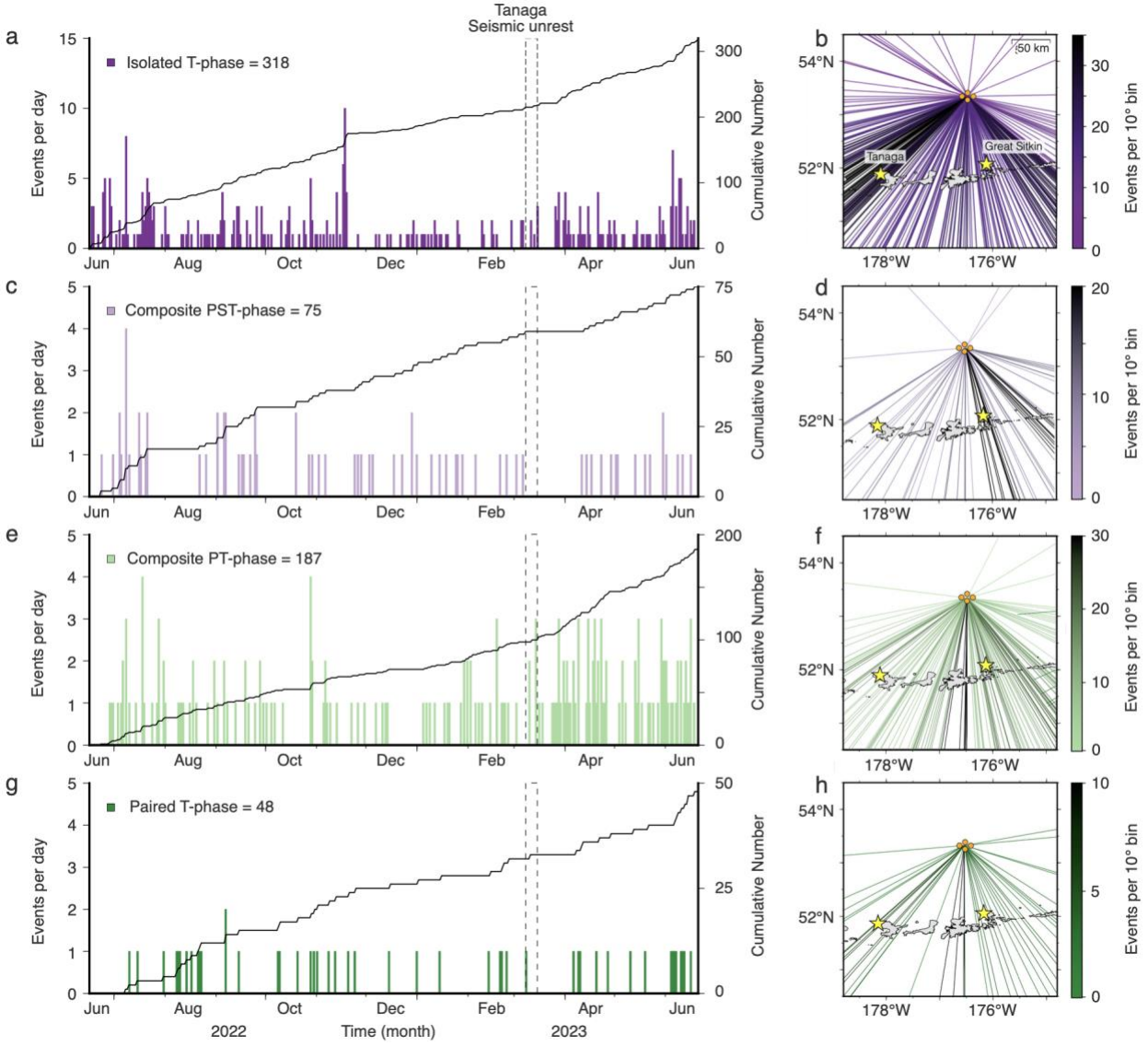

372

373 **Figure 5**: Number daily events (bars) and cumulative total (black line), and maps of back-azimuths
374 (shaded by number of events in 10° bins) for: **a-b)** isolated T-phases, **c-d)** composite PST-phases,
375 **e-f)** composite PT-phases, and **g-h)** paired T-phases. Dashed rectangle at the start of March 2023
376 outlines the third episode of Tanaga seismic unrest.

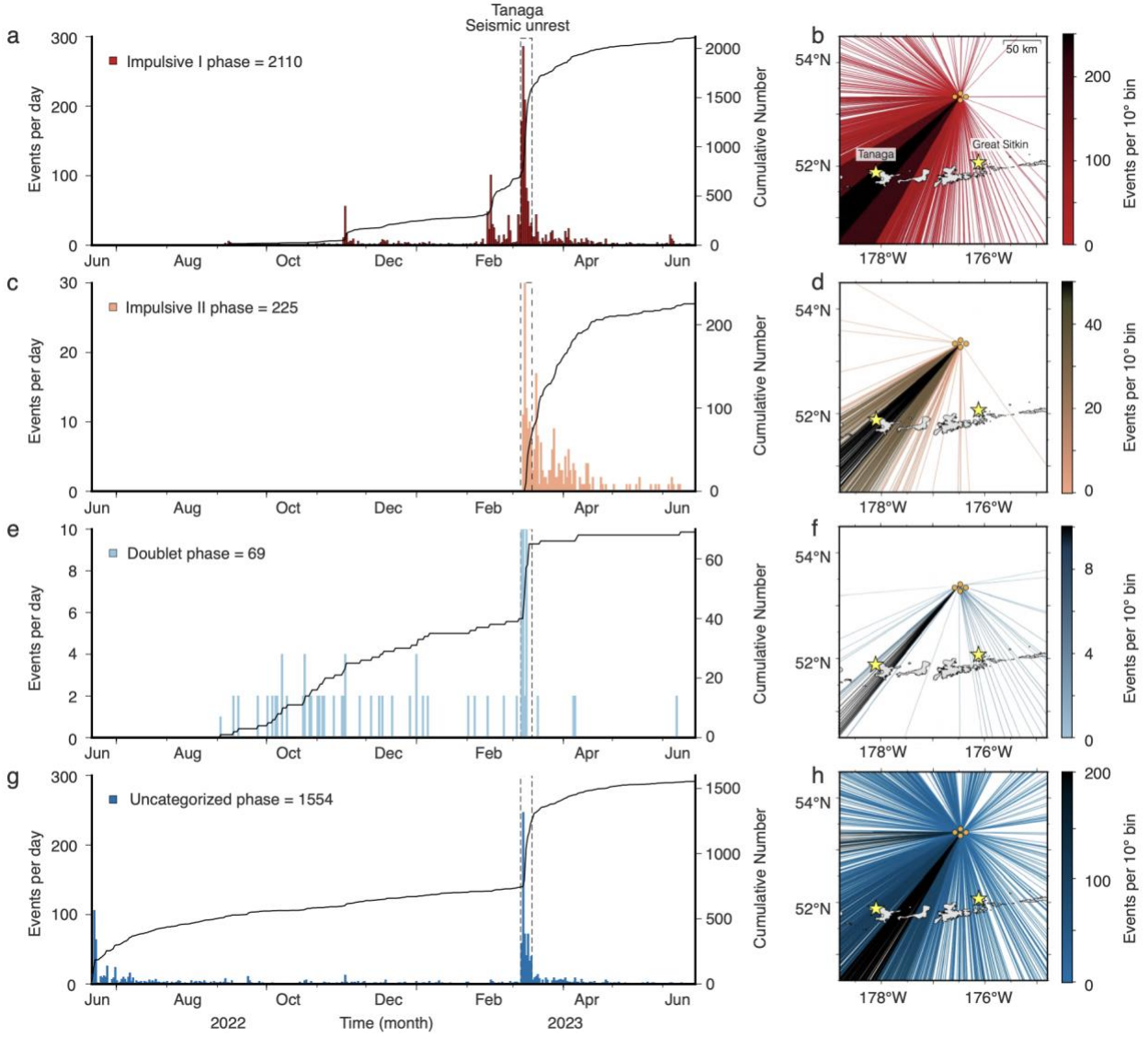

Figure 6: Number of daily events (bars) and cumulative total (black line), and maps of back-azimuths (shaded by number of events in 10° bins): **a-b)** impulsive I phases, **c-d)** impulsive II phases followed by multiple phases, **e-f)** doublet phases, and **g-h)** uncategorized phases. Dashed rectangle at the start of March 2023 outlines the third episode of Tanaga seismic unrest.

3.4 Matched events and rise time of hydroacoustic signals

The rise time of T-phases can provide valuable insights into the depth and source characteristics of their causative seismic events (e.g., Schreiner et al., 1995; Dziak and Fox, 1999; Dziak et al.,

2005). Defined as the time interval between a signal's onset (above noise level) and its maximum amplitude (e.g., Williams et al., 2006), rise time reflects the interaction of seismic waves with the seafloor before their acoustic conversion. Seismic waves propagating through Earth's crust from deeper events will typically intersect a larger portion of the ocean floor, resulting in longer rise times as the acoustic energy scatters or refracts before reaching the hydrophones (Schreiner et al., 1995). Large or deep earthquakes typically exhibit T-phase arrivals with rise times greater than 15 s, and prolonged decays often exceeding 30 s. In contrast, shallow events tend to generate shorter rise times, typically just a few seconds (Williams et al., 2006), and can even have an impulsive character (e.g., Tepp et al., 2020).

By comparing depths of matched events and rise times, we can explore possible connections. After matching the hydroacoustic catalog to the USGS catalog along the Aleutian Arc, we found 565 T-phase matches and 2,609 short-duration matches. The mean rise time of all 628 T-phase events (combining isolated, composite PST, PT and paired) was ~22 s (Table 1; Figure S7), suggesting that the source events may have been relatively deep, coupling energy over a relatively wide region of the ocean floor. Of these 628 events, 565 (89%) matched with USGS catalog events. Of these, one group of 465 matched events had a mean depth of 49.7 ± 43.0 km (with median of 35 km as most of the events were at this depth) and were spatially distributed along the trench (Table S3 and Figure S8). Notably, 356 of these matched events occurred at depths exceeding 20 km, with several originating at depths greater than 100 km. These observations suggest that longer rise times may correspond to deeper source events, possibly within the lower crust, deeper subduction interface, or upper mantle. Another group of 56 matched events showed back-azimuth towards Tanaga island and they had a mean depth of 3.6 $\pm$ 3.2 km (Figure S6a). One thing to note here is that only the isolated T-phases matched with seismic events along Tanaga. The remaining 44 events (mean depth of 13.5 $\pm$ 3.4 km) matched with events having azimuths toward Great Sitkin Island (Figure S9).

In contrast to the T-phase events, the impulsive I and II, doublet and uncategorized events had mean rise times of ~2 s, ~4 s, ~3.3 s and ~6 s, respectively. The relative difference of rise time between impulsive I and uncategorized events also helped us to consider them as two separate

categories. This short rise time could indicate shallow depths of these source events. The 3,958 short duration events yielded 2,609 (~66%) matched events in the USGS catalog. Of these, one group of 1,002 matched events had a mean depth of 16.4 $\pm$ 12.6 km (Table 1, S3 and Figure S10), suggesting that many originated in the upper crust or at shallow subsurface depths. The remaining 1,607 matched events showed back-azimuth towards Tanaga Island with a mean depth of 4.0 $\pm$ 2.8 km (Figure S11). Also, none of the short-duration events did not match with seismic events near Great Sitkin Island. These findings support the interface that shorter hydroacoustic rise times are indicative of shallower seismic source regions.

Among the short-duration events related to Tanaga seismicity, the rise times of doublet phases exhibited significant variability, being higher before the third episode of unrest in March (~4 s) and gradually decreasing during the unrest (Figure 7a), which could suggest a shift towards shallower source depths as unrest progressed. The matched seismic events for this category were consistently shallow, with depths less than 3 km (Figure 7c). Additionally, we computed the time difference between individual phases of the doublet signals and averaged them over a calendar month. The mean time difference was greater than 40 seconds before the unrest, with a higher 2σ standard deviation, whereas during the unrest, the time difference decreased to ~32 seconds, with lower variability (Figure 7b). This reduction in time difference could be accounted for two plausible scenarios. First, the alterations in the acoustic reflector(s) properties over time, possibly due to creation of new fractures or the reactivation of existing faults, that could affect seismic to hydroacoustic conversion zones. Second, reduction in the temporal separation associated with an increase in repeated ruptures at the same source or near-simultaneous activity from the closely spaced adjacent sources.

Hydroacoustic signals		**Matched seismic events from the USGS catalog**					
Hydroacoustic signal type	**Mean Rise time (s)**	**Along the trench**		**Near Tanaga Island**		**Near Great Sitkin Island**	
		% Matched	**Depth (km)**	**% Matched**	**Depth (km)**	**% Matched**	**Depth (km)**
Isolated T-phase	21.8 ± 2.8	78%	47.1 $\pm$ 41.1	9%	3.6 $\pm$ 3.2	3%	13.1 $\pm$ 3.5
T-phases from composite PST	21.7 ± 3.1	71%	50.8 $\pm$ 45.8	-	-	4%	13.9 $\pm$ 3.6
T-phase from composite PT	21.7 ± 2.8	80%	48.6 $\pm$ 40.3	-	-	-	-
Paired T-phases	22.2 ± 2.2	67%	50.7 $\pm$ 44.2	-	-	-	-

Impulsive I phases	2.0 ± 0.6	19%	12.5 ± 9.3	48%	3.9 ± 2.8	-	-
Impulsive II phases	4.0 ± 0.9	25%	14.3 ± 11.2	45%	4.1 ± 2.3	-	-
Doublet	3.3 ± 1.0	39%	19.6 ± 15.2	46%	3.8 ± 1.7	-	-
Uncategorized	6.0 ± 1.5	24%	19.2 ± 14.7	28%	4.2 ± 2.7	-	-

Table 1: Mean rise time of all hydroacoustic signals from different types recorded on four hydrophones; uncertainties are +/- 1 standard deviation along with corresponding percentage and mean depths of matched seismic events along trench, near Tanaga and Great Sitkin Islands. The higher uncertainties in depth are due to skewed distribution of USGS catalog event depths.

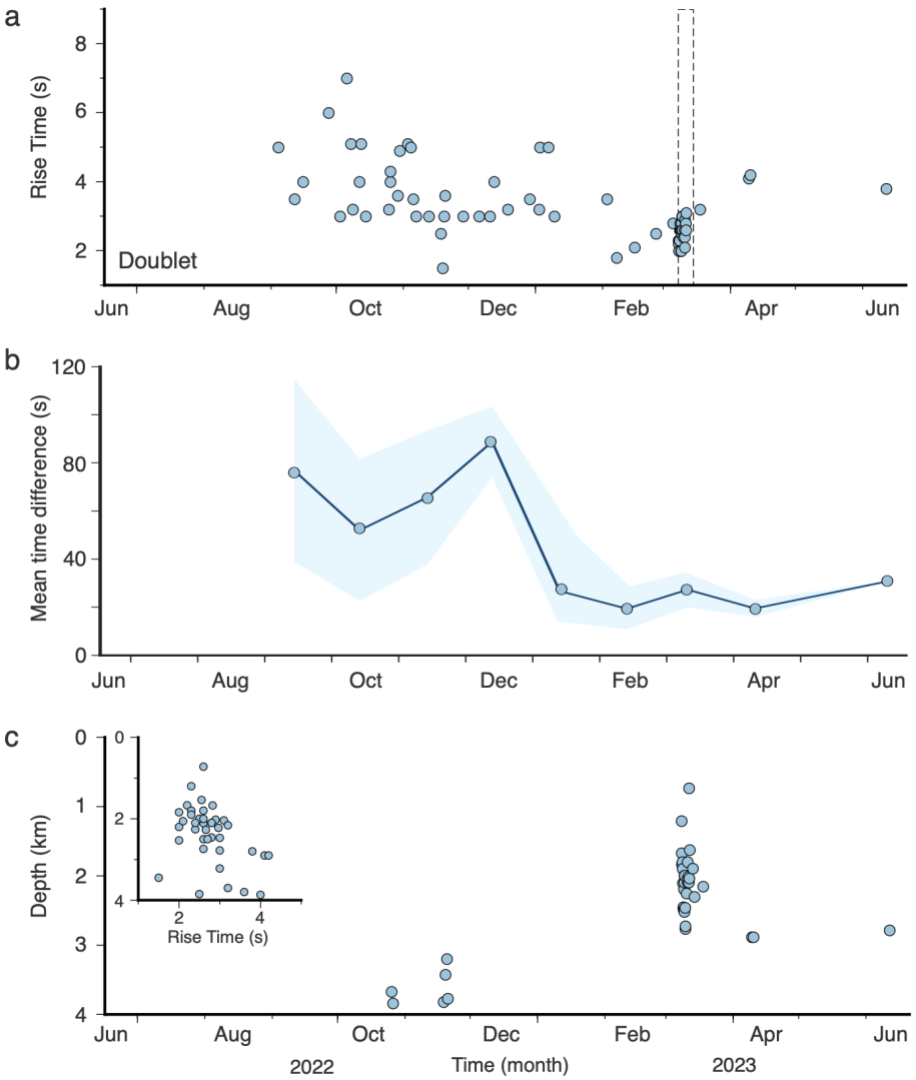

Figure 7: a) Rise time of doublet phases measured as time between onset and maximum amplitude of signal. **b)** Mean time difference between successive phases of doublet signal over a month (solid line) and corresponding standard deviation (shaded area). **c)** Depth of corresponding matched events found in USGS catalog, with an inset compares the depth with rise time

3.5 Received Level

To understand the nature of acoustic phases recorded between June 2022 and June 2023, we also consider RL obtained on each of the hydrophones. We measured the mean RL for all the hydrophones combined for each individual phase detected, which varied between 120 and 140 dB, demonstrating reliable measurements and a stable detection environment. The RL is based on the average PSD in a 10 s time window centered on the acoustic signal peak, but there is a limitation of amplitude clipping for some of the events (Figure S7d,f), which may not give true representation of signal energy.

We compared the temporal distribution of the RL of these phases. All types of hydroacoustic phases, except for doublets, had similar RL over the detection period (Figure 8). The doublet phases had a decrease in RL during the third period of Tanaga unrest, which also coincided with events with short rise time, suggesting potential changes in source characteristics or propagation conditions.

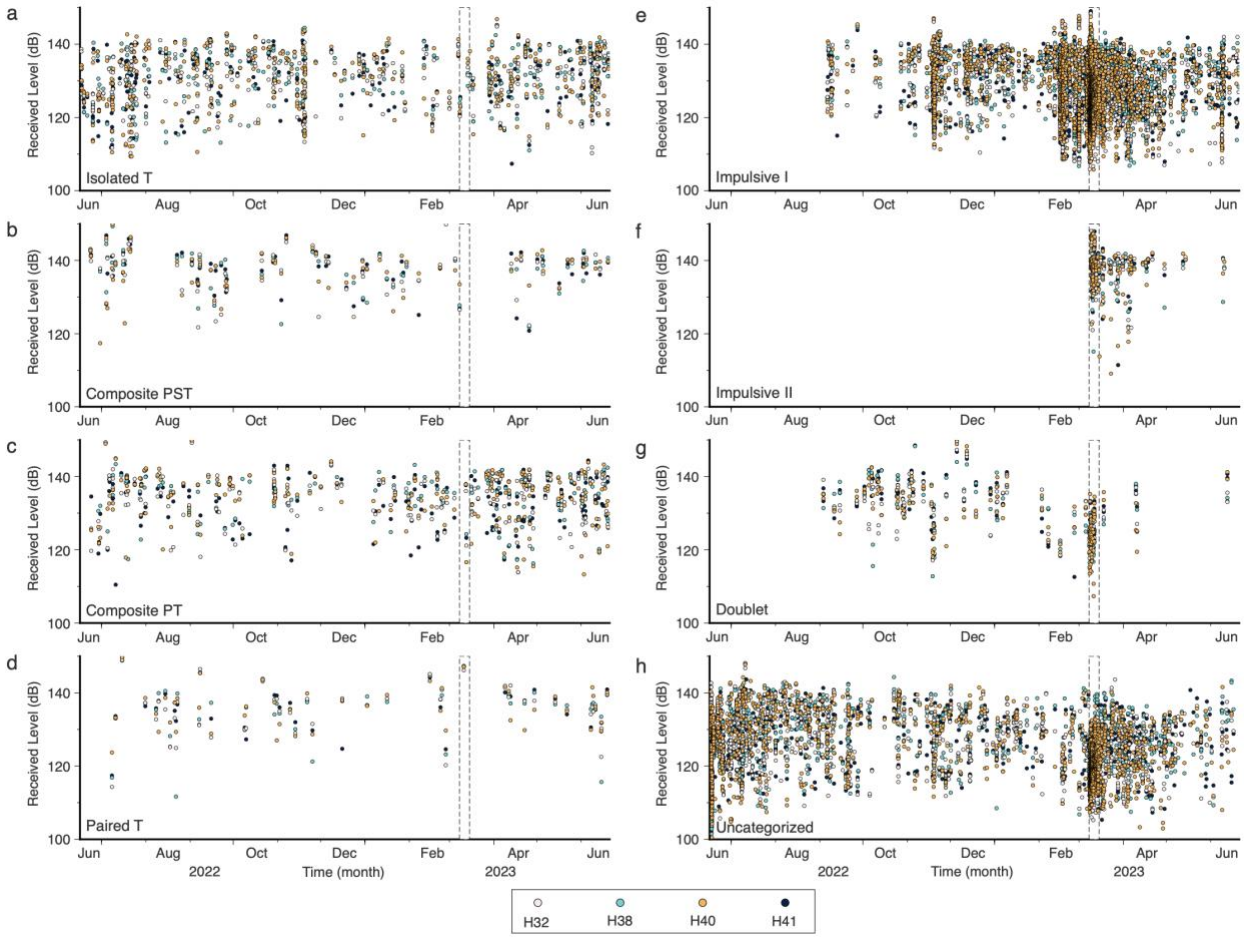

Figure 8: Received Levels on all four hydrophones (H32, H38, H40, and H41) for each event of the type: **a)** isolated T-phases, **b)** composite PST phases, **c)** composite PT phases, **d)** paired T-phases, **e)** impulsive I, **f)** impulsive II, **g)** doublet, and **h)** uncategorized phases.

We compared the local magnitude (M_L), depths, and received levels of the matched events found between the USGS and hydroacoustic catalogs between June 2022 and June 2023 (Figure 9). For impulsive I, impulsive II and uncategorized events, the relationship between M_L, depth, and RL appeared highly variable, preventing any definitive conclusions. In contrast, for doublet signals with short rise times, the matched seismic events were shallow, at depths < 5 km. These events also had smaller magnitudes, compared to matched events from the other short-duration phases (impulsive I, impulsive II and uncategorized; Figure 9). These small magnitude events possibly produced lower acoustic energy and contributed to lower RLs during the March 2023 unrest. The lower observed RLs for these shallow events may be attributed to their acoustic ray paths, which

could have a low incidence angle (relative to vertical, between subsurface and seafloor). Such geometries may enhance signal scattering and consequently lower RL (Williams et al., 2006; Lecoulant et al., 2019). For other impulsive phases, the wide range of RLs may be linked to the significant variability in depth and magnitude of matched seismic events (Figure 9). However, we note that no empirical relation can be established among RL, M_L and depth from this scattered distribution of RLs. This lack of correlation is probably due to uncertainties in the USGS catalog event locations, which hinders reliable estimation of transmission loss (TL). Because TL includes both cylindrical and spherical spreading components between the seafloor source and hydrophones, not accounting for it introduces uncertainty in comparing RL to seismic magnitude. While RL cannot be interpreted as a direct measure of acoustic source level, it remains a useful relative metric for comparing the relative strength of different hydroacoustic events. These findings highlight the complex interplay between source characteristics, propagation effects, and acoustic energy transmission in hydroacoustic phase generation. Future studies incorporating detailed propagation modeling and/or refined earthquake hypocenters may help further elucidate the mechanisms governing RL variations in different hydroacoustic phase types.

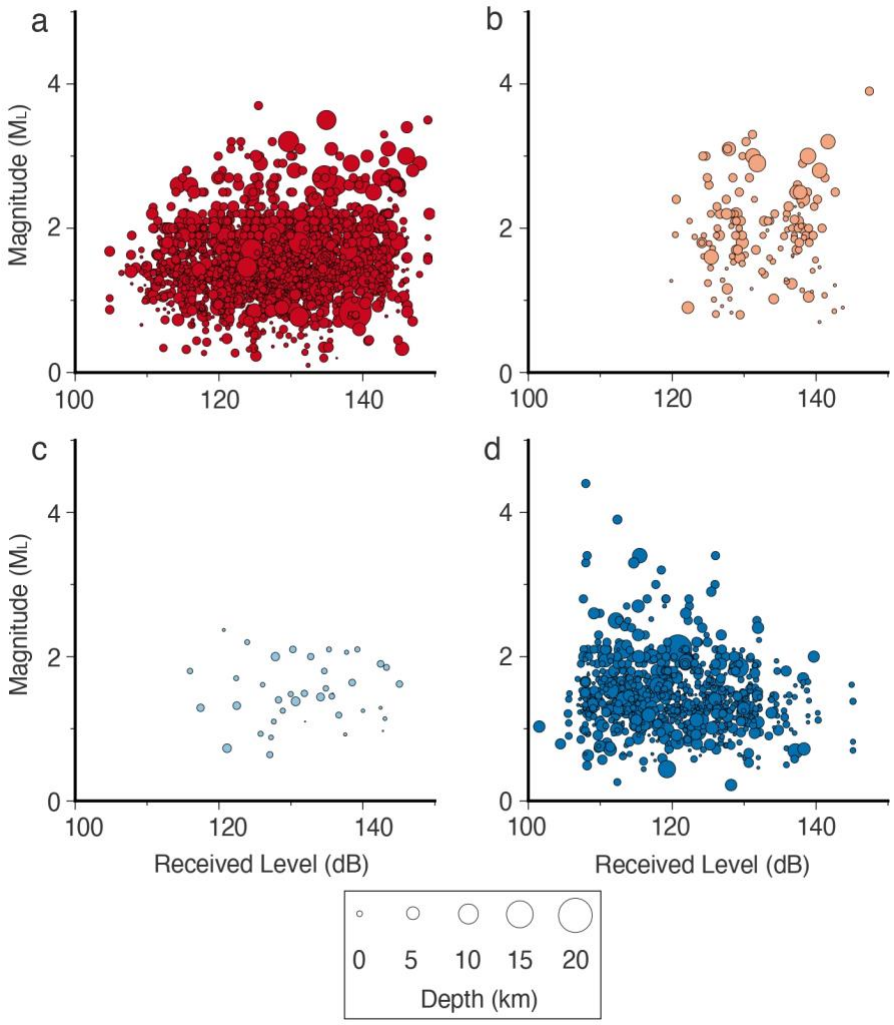

Figure 9: Comparison of local magnitude (M_L) and received levels for the matched events from USGS and hydroacoustic catalog for **a)** impulsive I, **b)** impulsive II, **c)** doublet, and **d)** uncategorized events. The depth variations are shown by different sizes of symbols.

4 Discussion

4.1 Nature of seismic and hydroacoustic activity near Tanaga Island

The seismic activity observed in episodes near Tanaga Island between November 2022 and March 2023 is non-eruptive unrest, likely driven by subsurface melt transport (Power et al., 2021; Godano et al., 2022). The temporal distribution of events in three distinct episodes predominantly feature earthquake swarms, characterized by numerous small-to-moderate

events clustered in time rather than a strong event followed by many smaller ones that is indicative of mainshock-aftershock sequences (Mogi, 1967; Passarelli et al., 2018; Tepp et al., 2020; Seropian et al., 2021; Vargas et al., 2023; Suarez et al., 2024). Swarm-like behavior generally characterizes magmatic systems undergoing subsurface processes like pressurization, fluid migration, or intrusive activity (e.g., Dziak et al., 2004b, Hainzl et al., 2004, Wilding et al., 2023).

This unrest can be categorized into three distinct activities. The first (18 to 21 November 2022) and the second (8 to 12 February 2023) episodes are characterized by shallow (< 10 km) depths of the USGS catalog events. These two episodes could reflect the short-term initiation activity period of the unrest. The time clustering of these events suggests a dynamic subsurface environment, driven by magmatic intrusions or fault reactivation (Heimisson and Segall, 2020; Parameswaran et al., 2023). Second, a sustained a saw the most intense period between 8-15 March 2023, characterized by 2,849 shallow (< 10 km) USGS catalog events (Figure S12). This period, although not culminating in a volcanic eruption, strongly suggests magma transport at shallow depths (White and McCausland, 2019; Gabrielson et al., 2024), akin to processes observed in other volcanic systems such as the Lesser Antilles (Feuillet et al., 2011), the Chiles-Cerro Negro volcanoes (Ebmeier et al., 2016) and São Jorge volcano-tectonic unrest (Suarez et al., 2024). The magma transport at shallow depths could pass through pre-existing faults or newly formed pathways due to intense activity (e.g., Bohnenstiehl et al., 2004; Scandone et al., 2007; Wilcock et al., 2016; Aswini et al., 2020; Gabrielson et al., 2024). Third, a decay period, where seismic activity waned after 15 March 2023, likely signifies the stabilization of the magmatic system following its transport. The redistribution of stress in the surrounding crust from the magma movement likely represents the decay period.

In this study, hydroacoustic monitoring also reveals these three distinct periods of elevated activity that coincide with the seismic activity distribution discussed above. Primarily, the short-duration signals provide a time-resolved proxy for chances in seismic activity and signal complexity across the unrest sequence. During the initiation activity, impulsive I hydroacoustic events dominated. These high frequency, short-duration phases are consistent with shallow

source processes based on the relation between their rise time and depth of matched seismic events (e.g., Bowers, 2001; Talandier and Okal, 2001). In the sustained phase, hydroacoustic activity dramatically increased, with 3,004 out of total 3,958 short-duration events occurring between 8-15 March 2023 (Figure 6). The simultaneous presence of all four hydroacoustic short-duration phases in this period may reflect complex subsurface processes. The broader variations in RLs and rise time of short-duration signals suggest heterogeneous source processes, which land-based seismic monitoring may not fully resolve. The decay phase also showed a decline in hydroacoustic signal counts and complexity, mirroring the waning seismicity and suggesting magmatic system-wide stress relaxation. Thus, hydroacoustic monitoring complements and enhances seismic observations by capturing the temporal evolution and signal diversity associated with shallow unrest processes. Importantly, hydroacoustic data could independently delineate the three stages of unrest, even in the absence of seismic catalogs, though without seismic locations, the spatial resolution and depth constraints remain limited.

When compared to Bogoslof Island, the only other Aleutian Arc volcanic system with documented hydroacoustic detections the signals recorded near Tanaga Island during the three activity episodes (initiation, sustained and decay) reveal a different reveal a different aspect of associated seismicity. At Bogoslof, Tepp et al. (2020) documented a progression from seismic swarms to explosive eruptive phases. In contrast, the Tanaga-associated episodes did not follow this pattern, underscoring the diverse range of activities that can be detected hydroacoustically. This distinction also highlights the variability in magmatic processes within the arc, emphasizing that while seismic swarms along with hydroacoustic signals can be indicators of magmatic activity, they do not always precede eruptions.

Overall, the seismicity near Tanaga Island is indicative of active subsurface magma transport. However, in further studies, relocating seismic events using a double-difference earthquake location algorithm (Waldhauser and Ellsworth, 2020), and combining it with hydroacoustic ray path modeling and spectral characterization (e.g., using SPECFM; Tromp et al., 2008) will help assess the acoustic coupling efficiency and the likely locations of seismic-to-acoustic conversions. This approach could constrain whether detected hydroacoustic phases originate from shallow

crustal ruptures, deeper sources, or multiple acoustic paths. During the March 2023 swarm, we observed a diversity of short-duration hydroacoustic signals; interpreting these in conjunction with improved seismic locations can provide insights into depth-dependent source processes and energy coupling variations that are not easily resolved from seismic data alone. This will enhance our understanding of the magma transport mechanism during the Tanaga unrest as well as the relation of this seismicity with individual volcanic centers of Tanaga Island (Lally et al., 2023).

4.2 Absence of signals from Great Sitkin and Semisopochnoi

The predominance of hydroacoustic signals originating from Tanaga, despite active eruptions at Great Sitkin and Semisopochnoi during the same time, could be attributed to different geological and oceanographic conditions that influence the propagation and detection of hydroacoustic waves. Semisopochnoi is situated at the southern end of Bowers Ridge, to the west of Tanaga (Figure 1). The elevated bathymetry of Bowers Ridge likely scatters acoustic waves, dispersing the energy in multiple directions and thereby reducing the efficiency of signal transmission to the hydrophone array (Figure S13; Williams et al., 2006). This attenuating effect may explain why we did not detect signals originating from Semisopochnoi.

In contrast, Great Sitkin and Tanaga are positioned in similar geographical conditions relative to the hydrophone array. There is no significant change in the elevation along the path towards the hydrophone network for both the volcanic islands, and they have similarly steep slopes (Figure S13). Of the total 4,586 hydroacoustic events detected, 1,663 (~36%) were matched with USGS catalog events near Tanaga Island, compared to 44 events (~1%) originating near Great Sitkin. This discrepancy likely reflects the significantly greater number of seismic events reported in the USGS catalog near Tanaga (> 4,000) compared to Great Sitkin (<200). Although both islands were active during the observation period (unrest at Tanaga and eruption at Great Sitkin), the limited earthquake seismicity at Great Sitkin appears to be the primary factor governing the low number of hydroacoustic matches. The spatial distribution of matched events at both Tanaga and Great Sitkin is scattered across the islands (Figures S9 and S11), with no consistent pattern suggesting localized coupling enhancements. This suggest that there is no fundamental difference in

586 acoustic coupling efficiency or any favorable geometry for seismic-to-acoustic conversion near
587 either of the islands.

588 Additionally, the depths of seismic events also likely contribute to the reduced number of events
589 at Great Sitkin. The unmatched events near Great Sitkin occurred at depths exceeding 20 km
590 (Figure S9), where seismic energy may be less effectively converted into acoustic by directing
591 energy along less favorable paths or leading to increased attenuation before reaching the
592 seafloor. In contrast, events near Tanaga were at < 20 km depth, possibly facilitating stronger
593 acoustic coupling. This pattern is consistent with observations from the 2016-17 Bogoslof
594 Island eruption, during which events with depth < 20 km generated acoustic signals that travelled
595 over ~700 km and were recorded by seismometers deployed on Tanaga Island (Tepp et al., 2020).

596 **5 Conclusions**

597 This study presents a detailed analysis of Tanaga seismic unrest along the Aleutian Arc using
598 hydroacoustic data from four hydrophones deployed in the Bering Sea, in conjunction with the
599 USGS seismic catalog. A total of 4,586 acoustic signals were detected and classified into two
600 primary types, T-phases and short-duration impulsive phases, based on signal duration. T-phase
601 signals, characterized by spindle-shape waveforms and appearing in both isolated and composite
602 forms. Apart from a few isolated T-phases, most of the T-phases (including composite events)
603 showed no correlation with Tanaga seismic unrest recorded by land-based networks. Based on
604 the correlation of the high rise time of these T-phase with the depths and location of matched
605 seismic events, these events are likely related to deeper source events, possibly within the lower
606 crust, deeper subduction interface, or upper mantle. In contrast, a notable increase in short-
607 duration (~10 s) impulsive signals coincided with seismic unrest, with back-azimuth analysis
608 indicating that approximately 60% of these events originated from Tanaga Island. Most of these
609 events coeval with events recorded by the land-based networks (in the USGS catalog), indicating
610 a strong association between the hydroacoustic signals and seismic activity. The hydroacoustic
611 activity rate sharply increased during the 8-15 March 2023 episode, contributing to the strong
612 and intense episode of seismic unrest. Doublet impulsive signals showed decreasing rise times
613 and RLs that were consistent with low magnitude and shallow seismic events, a pattern

potentially consistent with shallow magmatic processes during the same time. The rest of the impulsive events showed a wide range of RLs probably due to significant variability in depth and magnitude of matched seismic events. The presence of three distinct periods (initiation, sustained, and decay), both in the hydroacoustic impulsive and seismic events catalogs, again suggest that shallow magmatic processes are involved during the Tanaga unrest. Further comparisons between the hydroacoustic detections and relocated seismicity will strengthen the interpretation of magma transport beneath the Tanaga volcanic center, and others in similar arc settings.

Acknowledgments

This work was supported by the NOAA Ocean Exploration Program and by a Green Foundation Scholarship from the Institute of Geophysics and Planetary Physics, UC San Diego. We are grateful to Eleanor R. H. Mestel and an anonymous reviewer for their constructive comments which helped us to improve our work. We thank Lauren Roche, Mike Craig, Jay Turnbull, and Phyllis Stabeno for leading the hydrophone deployment and recovery efforts. Also special thanks to the Captains and crew of the USCG M/V Cypress and the R/V Aquila for their expert skills at sea in support of this project. This is NOAA-PMEL contribution #5727.

Open Research

All hydrophone data used in this study will be made publicly available via the NOAA NCEI passive acoustics portal: https://www.ncei.noaa.gov/products/passive-acoustic-data. The hydroacoustic signals were picked using Seasick software developed at NOAA-PMEL. The hydroacoustic catalog including station coordinates used in this study are archived at Zenodo via https://doi.org/10.5281/zenodo.14827943 (Inagle et al., 2025). Seismic event catalog is obtained from the United States Geological Survey catalog (https://earthquake.usgs.gov/earthquakes/search/), last accessed: 15 November 2024. Bathymetric data were obtained from the Global Multi-Resolution Topography compilation via https://www.gmrt.org/GMRTMapTool/ (Ryan et al., 2009). Temperature and salinity data to compute the water velocity were obtained from World Ocean Atlas (NCEI Accession 0270533;

642 Reagan et al., 2024). Figures made with the Generic Mapping Tools (Wessel et al., 2019). The
643 codes for preliminary processing of hydroacoustic catalog and computing back-azimuth of signals
644 is available online (Ingale, 2025).

645

646 **Declaration of competing interests**

647 The authors acknowledge that there are no conflicts of interest recorded.

648 **References**

649 Alaska Earthquake Center, Univ. of Alaska Fairbanks. (1987). *Alaska Geophysical Network* [Data
650 set]. International Federation of Digital Seismograph Networks. https://doi.org/10.7914/SN/AK,
651 last accessed: 15 November, 2024

652 Alaska Volcano Observatory/USGS. (1988). *Alaska Volcano Observatory* [Data set]. International
653 Federation of Digital Seismograph Networks. https://doi.org/10.7914/SN/AV, last accessed: 15
654 November, 2024

655 Albuquerque Seismological Laboratory (ASL)/USGS. (1990). United States National Seismic
656 Network [Data set]. International Federation of Digital Seismograph Networks.
657 https://doi.org/10.7914/SN/US, last accessed: 15 November, 2024

658 Aswini, K. K., Dewangan, P., Kamesh Raju, K. A., Yatheesh, V., Singha, P., Arya, L., and Reddy, T.
659 R. (2020). Sub-surface magma movement inferred from low-frequency seismic events in the off-
660 Nicobar region, Andaman Sea. *Scientific Reports* 10, 21219. https://doi.org/10.1038/s41598-
661 020-78216-2

662 Bohnenstiehl, D. R., Dziak, R. P., Tolstoy, M., Fox, C. G., & Fowler, M. (2004). Temporal and spatial
663 history of the 1999-2000 Endeavour Segment seismic series, Juan de Fuca Ridge. *Geochemistry,*
664 *Geophysics, Geosystems*, *5(9)*. https://doi.org/10.1029/2004GC000735

665 Buurman, H., Nye, C. J., West, M. E., and Cameron, C. (2014). Regional controls on volcano
666 seismicity along the Aleutian arc. *Geochemistry, Geophysics, Geosystems*, *15*(4), 1147–1163.
667 https://doi.org/10.1002/2013GC005101

668 Benz, H. M., Herman, M., Tarr, A. C., Hayes, G. P., Furlong, K. P., Villaseñor, A., Dart, R. L., and
669 Rhea, S. (2010). Seismicity of the Earth 1900-2010, Aleutian arc and vicinity. *U.S. Geological*
670 *Survey Open-File Report 2010-1083-B*. https://doi.org/10.3133/ofr20101083B

671 Cameron, C. E., Bull, K. F., and Macpherson, A. E. (2023). Recently active volcanoes of Alaska:
672 Alaska Division of Geological & Geophysical Surveys Miscellaneous Publication 133 v. 6, 2 sheets.
673 https://doi.org/10.14509/31086

674 Coombs, M. L., Larsen, J. F., and Neal, C. A. (2018). Postglacial eruptive history and geochemistry
675 of Semisopochnoi volcano, western Aleutian Islands, Alaska: U.S. Geological Survey Scientific
676 Investigations Report 2017-5150, 32 p., https://doi.org/10.3133/sir20175150

677 Dziak, R. P. (2001). Empirical relationship of T-wave energy and fault parameters of northeast
678 Pacific Ocean earthquakes. *Geophysical Research Letters*, *28*(13), 2537-2540.
679 https://doi.org/10.1029/2001GL012939

680 Dziak, R. P., Bohnenstiehl, D. R., Matsumoto, H., Fox, C. G., Smith, D. K., Tolstoy, M., Lau, T. K.,
681 Haxel, J. H. and Fowler, M. J. (2004a). P-and T-wave detection thresholds, Pn velocity estimate,
682 and detection of lower mantle and core P-waves on ocean sound-channel hydrophones at the
683 Mid-Atlantic Ridge. *Bulletin of the Seismological Society of America*, *94*(2), 665-677.
684 https://doi.org/10.1785/0120030156

685 Dziak, R. P., Smith, D. K., Bohnenstiehl, D. R., Fox, C. G., Desbruyeres, D., Matsumoto, H., Tolstoy,
686 M., and Fornari, D. J. (2004b). Evidence of a recent magma dike intrusion at the slow spreading
687 Lucky Strike segment, Mid-Atlantic Ridge. *Journal of Geophysical Research: Solid Earth*, *109*(B12).
688 https://doi.org/10.1029/2004JB003141

689 Dziak, R. P., and Fox, G. C. (1999). The January 1998 earthquake swarm at axial volcano, Juan de
690 Fuca Ridge: hydroacoustic evidence of a seafloor volcanic activity, *Geophysical Research Letters*
691 26, 3429-3432. https://doi.org/10.1029/1999GL002332

692 Dziak, R. P., Lee, W. S., Haxel, J. H., Matsumoto, H., Tepp, G., Lau, T. K., Roche, L., Yun, S., Lee, C-
693 K., Lee, J and Yoon, S. T. (2019). Hydroacoustic, meteorologic and seismic observations of the
694 2016 Nansen ice shelf calving event and iceberg formation. *Frontiers in Earth Science*, *7*, 183.
695 https://doi.org/10.3389/feart.2019.00183

696 Dziak, R., Matsumoto, H., Haver, S., Mellinger, D., Roche, L., Haxel, J., Stalin, S., Meinig, C.,
697 Kohlman, K., Sremba, A., Gedamke, J., Hatch, L., and Van Parijs, S. (2023). PMEL Passive Acoustics
698 Research: Quantifying the Ocean Soundscape from Whales to Wave Energy. *Oceanography*.
699 https://doi.org/10.5670/oceanog.2023.203

700 Dziak, R. P., Park, M., Matsumoto, H., and Byun, S. K. (2005). Hydroacoustic records and a
701 numerical model of the source mechanism from the first historical eruption of Anatahan Volcano,
702 Mariana Islands. *Journal of volcanology and geothermal research*, *146*(1-3), 86-101.
703 https://doi.org/10.1016/j.jvolgeores.2004.12.009

704 Ebmeier, S. K., Elliott, J. R., Nocquet, J. M., Biggs, J., Mothes, P., Jarrín, P., Yépez, M., Aguaiza, S.,
705 Lundgren, P., and Samsonov, S. V. (2016). Shallow earthquake inhibits unrest near Chiles–Cerro
706 Negro volcanoes, Ecuador–Colombian border. *Earth and Planetary Science Letters*, *450*, 283-291.
707 https://doi.org/10.1016/j.epsl.2016.06.046

708 Feuillet, N., Beauducel, F., & Tapponnier, P. (2011). Tectonic context of moderate to large
709 historical earthquakes in the Lesser Antilles and mechanical coupling with volcanoes. *Journal of*
710 *Geophysical Research: Solid Earth*, *116*(B10). https://doi.org/10.1029/2011JB008443

711 Fox, C. G., Matsumoto, H., and Lau, T. A. (2001). Monitoring Pacific Ocean seismicity from an
712 autonomous hydrophone array. *Journal of Geophysical Research: Solid Earth*, *106*(B3), 4183–
713 4206. https://doi.org/10.1029/2000JB900404

714 Gabrielson, C., Caplan-Auerbach, J., and Power, J. A. (2024). Resolving the Magmatic Structure of
715 the Tanaga Volcanic Cluster, Aleutian Arc, Alaska, Using Double Difference Earthquake Relocation
716 and Tomography. AGU Fall Meeting Abstracts, 9-13 December, 2024, Washington DC, USA.
717 https://agu.confex.com/agu/agu24/meetingapp.cgi/Paper/1537166

718 Global Volcanism Program (2023a). Report on Tanaga (United States) (Sennert, S., ed.). Weekly
719 Volcanic Activity Report, 8 March-14 March, 2023. Smithsonian Institution and US Geological
720 Survey.

721 Global Volcanism Program (2023b). Report on Great Sitkin (United States) (Venzke, E., ed.).
722 Bulletin of the Global Volcanism Network, 48:11. Smithsonian Institution.

723 Global Volcanism Program (2023c). Report on Semisopochnoi (United States) (Bennis, K. L., and
724 Andrew, B., eds.). Bulletin of the Global Volcanism Network, 48:6. Smithsonian Institution.

725 Godano, C., Tramelli, A., Mora, M., Taylor, W., & Petrillo, G. (2023). An analytic expression for the
726 volcanic seismic swarms occurrence rate. A case study of some volcanoes in the world. *Earth and*
727 *Space Science*, *10*(2), e2022EA002534. https://doi.org/10.1029/2022EA002534

728 Hainzl, S. (2004). Seismicity patterns of earthquake swarms due to fluid intrusion and stress
729 triggering. *Geophysical Journal International*, 159(3), 1090–
730 1096. https://doi.org/10.1111/j.1365-246X.2004.02463.x

731 Haxel, J. H., Dziak, R. P., and Matsumoto, H. (2013). Observations of shallow water marine
732 ambient sound: The low frequency underwater soundscape of the central Oregon coast. *The*
733 *Journal of the Acoustical Society of America 133*(5), 2586-2596.
734 https://doi.org/10.1121/1.4796132

735 Heimisson, E. R. and, Segall, P. (2020). Physically consistent modeling of Dike-induced
736 deformation and seismicity: Application to the 2014 Bárðarbunga Dike, Iceland. *Journal of*
737 *Geophysical Research: Solid Earth,* 125(2), e2019JB018141
738 https://doi.org/10.1029/2019JB018141

739 Herrick, J. A., Neal, C. A., Cameron, C. E., Dixon, J. P., and McGimsey, R. G. (2014). 2012 volcanic
740 activity in Alaska: Summary of events and response of the Alaska Volcano Observatory. *U.S.*
741 *Geological Survey Scientific Investigation Report 2014-5160*.
742 https://doi.org/10.3133/sir20145160

743 Ingale, V. V. (2025). Hydroacoustic Catalog Processing Toolkit: V0.1 (Version 0.1) [Software].
744 Zenodo. https://doi.org/10.5281/zenodo.15485743

745 Ingale, V. V., Tepp, G., Dziak, R. P., and Parnell-Turner, R. (2025). Hydroacoustic catalog along the
746 Aleutian arc in 2022-2023 [Data set]. Zenodo. https://doi.org/10.5281/zenodo.14827943

747 Janiszewski, H. A., Abers, G. A., Shillington, D. J., and Calkins, J. A. (2013). Crustal structure along
748 the Aleutian island arc: New insights from receiver functions constrained by active-source data.
749 *Geochemistry, Geophysics, Geosystems*, *14*(8), 2977–2992. https://doi.org/10.1002/ggge.20211

750 Jensen, F. B., W. A. Kuperman, M. B. Porter, and H. Schmidt (1994). Computational Ocean
751 Acoustics, American Institute of Physics, New York, 14-15. https://doi.org/10.1007/978-1-4419-
752 8678-8

753 Jiang, Y., González, P. J., and Bürgmann, R. (2022). Subduction earthquakes controlled by
754 incoming plate geometry: The 2020 M > 7.5 Shumagin, Alaska, earthquake doublet. *Earth and*
755 *Planetary Science Letters*, *584*, 117447. https://doi.org/10.1016/j.epsl.2022.117447

756 Kutschale H (1969). Arctic hydroacoustics. Arctic 22(3):246–264.
757 https://doi.org/10.14430/arctic3218

758 Lallemant, H. G. A. (1996). Displacement partitioning and arc-parallel extension in the Aleutian
759 volcanic island arc. *Tectonophysics*, *256*(1–4), 279–293. https://doi.org/10.1016/0040-
760 1951(95)00171-9

761 Lally, K. F., Caplan-Auerbach, J., and Power, J. A. (2023). Volcanic and tectonic sources of
762 seismicity near the Tanaga volcanic cluster, Alaska. *Geochemistry, Geophysics, Geosystems*,
763 24(6), e2023GC010891. https://doi.org/10.1029/2023GC010891

764 Larsen, J. F. (2016). Unraveling the diversity in arc volcanic eruption styles: Examples from the
765 Aleutian volcanic arc, Alaska. *Journal of Volcanology and Geothermal Research*, *327*, 643–668.
766 https://doi.org/10.1016/j.jvolgeores.2016.09.008

767 Lecoulant, J., Guennou, C., Guillon, L., and Royer, J.-Y. (2019). Three-dimensional modeling of
768 earthquake generated acoustic waves in the ocean in simplified configurations. *The Journal of*
769 *the Acoustical Society of America*, 146(3):2113–2123. https://doi.org/10.1121/1.5126009

770 Li, Z. (2021). Recent advances in earthquake monitoring I: Ongoing revolution of seismic
771 instrumentation. *Earthquake science*, *34*(2), 177-188. https://doi.org/10.29382/eqs-2021-0011

772 Mogi, K. (1967). Earthquakes and fractures, *Tectonophysics* 5, 35- 55.
773 https://doi.org/10.1016/0040-1951(67)90043-1

774 Mortera-Gutiérrez, C. A., Scholl, D. W., and Carlson, R. L. (2003). Fault trends on the seaward
775 slope of the Aleutian Trench: Implications for a laterally changing stress field tied to a westward
776 increase in oblique convergence. *Journal of Geophysical Research: Solid Earth*, *108*(B10),
777 2001JB001433. https://doi.org/10.1029/2001JB001433

778 Murray, J. J., Matus, A. V., Hudnall, L. A., Krueger, A. J., Haynes, J. A., and Pippin, M. R. (2009).
779 Volcanic ash impacts on air traffic from the 2009 Mt. Redoubt eruption. In *AGU Fall Meeting*
780 *Abstracts*, V31A-1949. https://ui.adsabs.harvard.edu/abs/2009AGUFM.V31A1949M

781 Orr, T. R., Cameron, C. E., Dietterich, H. R., Loewen, M. W., Lopez, T., Lyons, J. J., Nakai, J., Power,
782 J. A., Searcy, C., Tepp, G., and Waythomas, C. W. (2024). 2020 Volcanic activity in Alaska -
783 Summary of events and response of the Alaska Volcano Observatory. *U.S. Geological Survey*
784 *Scientific Investigations Report 2024-5004*. https://doi.org/10.3133/sir20245004

785 Orr, T. R., Dietterich, H. R., Fee D., Girona, T., Grapenthin, R., Haney, M. M., Loewen, M. W., Lyons,
786 J. J., Power, J. A., Schwaiger, H. F., Schneider, D. J., Tan, D., Toney, L., Wasser, V. K., and
787 Waythomas, C. F. (2024b). 2021 Volcanic activity in Alaska and the Commonwealth of the
788 Northern Mariana Islands - Summary of events and response of the Alaska Volcano Observatory:
789 U.S. Geological Survey Scientific Investigations Report 2024-5014.
790 https://doi.org/10.3133/sir20245014

791 Parameswaran, R. M., Bjarnason, I. T., and Thorbjarnardóttir, B. S. (2023). Evolution of Stresses
792 Over Conjugate Faults in Hjalli-Ölfus, South Iceland. *Journal of Geophysical Research: Solid*
793 *Earth*, *128*(3), e2022JB026201. https://doi.org/10.1029/2022JB026201

794 Passarelli, L., Heryandoko, N., Cesca, S., Rivalta, E., Rasmid, Rohadi, S., Dahm, T., and Milkereit,
795 C. (2018). Magmatic or not magmatic? The 2015–2016 seismic swarm at the long-dormant Jailolo
796 volcano, West Halmahera, Indonesia. *Frontiers in Earth Science*, *6*, 79.
797 https://doi.org/10.3389/feart.2018.00079

798 Power, J. A., Roman, D. C., Lyons, J. J., Haney, M. M., Rasmussen, D. J., Plank, T., Nicolaysen, K.
799 P., Izbekov, P., Werner, C., and Kaufman, A. M. (2021). Volcanic seismicity beneath Chuginadak
800 Island, Alaska (Cleveland and Tana volcanoes): Implications for magma dynamics and eruption
801 forecasting. *Journal of Volcanology and Geothermal Research*, *412*, 107182.
802 https://doi.org/10.1016/j.jvolgeores.2021.107182

803 Reagan, J. R., Boyer, T. P., García, H. E., Locarnini, R. A., Baranova, O. K., Bouchard, C., Cross, S. L.,
804 Mishonov, A. V., Paver, C. R., Seidov, D., Wang, Z., Dukhovskoy, D. (2024). World Ocean Atlas
805 2023. *NOAA National Centers for Environmental Information*. Dataset: NCEI Accession 0270533

806 Royer, J.-Y., Chateau, R., Dziak, R. P. and Bohnenstiehl, D. R. (2015). Seafloor seismicity, Antarctic
807 ice-sounds, cetacean vocalizations and long-term ambient sound in the Indian Ocean basin,
808 *Geophysical Journal International* 202, 748–762. https://doi.org/10.1093/gji/ggv178

809 Ryan, W. B. F., Carbotte, S. M., Coplan, J. O., O'Hazra, S., Melkonian, A., et al. (2009), Global Multi-
810 Resolution Topography synthesis, *Geochemistry Geophysics Geosystems*, 10, Q03014.
811 https://doi.org/10.1029/2008GC002332

812 Scandone, R., Cashman, K. V., and Malone, S. D. (2007). Magma supply, magma ascent and the
813 style of volcanic eruptions. *Earth and Planetary Science Letters*, *253*(3-4), 513-529.
814 https://doi.org/10.1016/j.epsl.2006.11.016

815 Schreiner, A.E., C. G. Fox, and R. P. Dziak (1995). Spectra and magnitudes of T-waves from the
816 1993 earthquake swarm on the Juan de Fuca Ridge, *Geophysical Research Letters*, 22, 139–142.
817 https://doi.org/10.1029/94GL01912.

818 Seropian, G., Kennedy, B.M., Walter, T.R., Ichihara, M., and Jolly, A. D. (2021). A review
819 framework of how earthquakes trigger volcanic eruptions. *Nature Communications* 12, 1004.
820 https://doi.org/10.1038/s41467-021-21166-8

821 Suarez, E. D., Meletlidis, S., Domínguez-Cerdeña, I., del Fresno, C., Perdiguer-Lopez, R., &
822 Poczatek-Stanczyk, M. (2024). São Jorge's Volcano-Tectonic Unrest in 2022: A Joint Interpretation
823 Through GNSS and Fully Automated Seismic Analysis. *Pure and Applied Geophysics*, 1-23.
824 https://doi.org/10.1007/s00024-024-03612-y

825 Teague, W. J., Carron, M. J., and Hogan, P. J. (1990). A Comparison Between the Generalized
826 Digital Environmental Model and Levitus climatologies. *Journal of Geophysical Research: Oceans*,
827 *95*(C5), 7167–7183. https://doi.org/10.1029/JC095iC05p07167

828 Tepp, G. (2024). Monitoring marine eruptions. US Geological Survey Scientific Investigations
829 Report 2024-5062-I. https://doi.org/10.3133/sir20245062I

830 Tepp, G. and Dziak, R. P. (2021). The Seismo-Acoustics of Submarine Volcanic Eruptions. Journal
831 of Geophysical Research: Solid Earth, 126(4), e2020JB020912.
832 https://doi.org/10.1029/2020JB020912

Tepp, G., Dziak, R. P., Haney, M. M., Lyons, J. J., Searcy, C., Matsumoto, H., and Haxel, J. (2020). Seismic and hydroacoustic observations of the 2016–17 Bogoslof eruption. *Bulletin of Volcanology*, *82*(1), 4. https://doi.org/10.1007/s00445-019-1344-3

Tromp, J., Komatitsch, D., and Qiny, L. (2008). Spectral-element and adjoint methods in seismology. *Communications in Computational Physics*, 3(1), 1–32. https://doi.org/2008CiCP-7840

Vargas, C. A., Caneva, A., Solano, J. M., Gulisano, A. M., and Villalobos, J. (2023). Evidencing Fluid Migration of the Crust during the Seismic Swarm by Using 1D Magnetotelluric Monitoring. *Applied Sciences*, *13*(4), 2683. https://doi.org/10.3390/app13042683

Waldhauser F. and Ellsworth, W. L. (2000). A double-difference earthquake location algorithm: Method and application to the northern Hayward fault. *Bulletin of Seismological Society of America*, 90, 1353-1368. https://doi.org/10.1785/0120000006

Wang, J., Lu, Z., Bekaert, D., Marshak, C., Govorcin, M., Sangha, S., Kennedy, J., and Gregg, P. (2023). Along-Arc Volcanism in the Western and Central Aleutian From 2015 to 2021 Revealed by Cloud-Based InSAR Processing. *Geophysical Research Letters*, *50*(23), e2023GL106323. https://doi.org/10.1029/2023GL106323

Wessel, P., Luis, J. F., Uieda, L., Scharroo, R., Wobbe, F., Smith, W. H. F., and Tian, D. (2019). The generic mapping Tools version 6. *Geochemistry Geophysics Geosystems*, 20(11), 5556–5564. https://doi.org/10.1029/2019GC008515

White, R. A., & McCausland, W. A. (2019). A process-based model of pre-eruption seismicity patterns and its use for eruption forecasting at dormant stratovolcanoes. *Journal of Volcanology and Geothermal Research*, *382*, 267-297. https://doi.org/10.1016/j.jvolgeores.2019.03.004

Wilcock, W. S. D., Tolstoy, M., Waldhauser, F., Garcia, C., Tan, Y. J., Bohnenstiehl, D. R., Caplan-Auerbach, J., Dziak, R. P., Arnulf, A. F., and Mann, M. E. (2016). Seismic constraints on caldera

857 dynamics from the 2015 Axial Seamount eruption. *Science*, *354*(6318), 1395–1399.
858 https://doi.org/10.1126/science.aah5563

859 Wilding, J. D., Zhu, W., Ross, Z. E., & Jackson, J. M. (2023). The magmatic web beneath Hawai
860 'i. *Science*, *379*(6631), 462-468. https://doi.org/10.1126/science.ade5755

861 Williams, C. M., Stephen, R. A., and Smith D. K. (2006). Hydroacoustic events located at the
862 intersection of the Atlantis (30°N) and Kane (23°40'N) Transform Faults with the Mid-Atlantic
863 Ridge, *Geochemistry Geophysics Geosystems* 7, Q06015, doi:
864 https://doi.org/10.1029/2005GC001127

865 Yang, X., and Gao, H. (2020). Segmentation of the Aleutian-Alaska Subduction Zone Revealed by
866 Full-Wave Ambient Noise Tomography: Implications for the Along-Strike Variation of Volcanism.
867 *Journal of Geophysical Research: Solid Earth*, *125*(11), e2020JB019677.
868 https://doi.org/10.1029/2020JB019677
869

Figure captions:

Figure 1: Locations of four hydrophones (orange circles) deployed by PMEL-NOAA in the Bering Sea, north of the Aleutian arc in 2022-2023. Yellow stars show volcanic centers that experienced unrest and eruption in 2022-2023 (Global Volcanism Program, 2023a, 2023b, 2023c). Black stars show volcanic centers that did not experience unrest. Bathymetry is from Ryan et al. (2009).

Figure 2: a) Earthquake density per km^2 between 16 June 2022 and 22 June 2023 on Tanaga Island obtained from USGS catalog (Alaska Earthquake Center, 1987; Alaska Volcano Observatory, 1988; Albuquerque Seismological Laboratory, 1990); relief is from Ryan et al. (2009). **b)** Histogram of number of events per day and the temporal distribution of **c)** local magnitudes and **d)** depths. Red histogram/dots show all the USGS events near Tanaga Island in 2022-2023 and blue histogram/dots show only USGS events with a hydroacoustic match.

Figure 3: Waveforms and spectrograms of representative signals: **a-b)** spindle-shaped isolated T-phase, **c-d)** composite PST phase, **e-f)** composite PT phase, **g-h)** paired T-phase after P and S, **i-j)** impulsive I phase, **k-l)** impulsive II phase followed by weak amplitude phases, **m-n)** doublet phase, and **o-p)** uncategorized phase having weak amplitudes and frequencies; waveforms are shown unfiltered.

Figure 4: Average power spectral density of randomly selected events for different types of signals: T-phases, impulsive I, impulsive II, doublet, and uncategorized phases.

Figure 5: Number daily events (bars) and cumulative total (black line), and maps of back-azimuths (shaded by number of events in 10° bins) for: **a-b)** isolated T-phases, **c-d)** composite PST-phases, **e-f)** composite PT-phases, and **g-h)** paired T-phases. Dashed rectangle at the start of March 2023 outlines the third episode of Tanaga seismic unrest.

Figure 6: Number of daily events (bars) and cumulative total (black line), and maps of back-azimuths (shaded by number of events in 10° bins): **a-b)** impulsive I phases, **c-d)** impulsive II phases followed by multiple phases, **e-f)** doublet phases, and **g-h)** uncategorized phases. Dashed rectangle at the start of March 2023 outlines the third episode of Tanaga seismic unrest.

Figure 7: a) Rise time of doublet phases measured as time between onset and maximum amplitude of signal. **b)** Mean time difference between successive phases of doublet signal over a month (solid line) and corresponding standard deviation (shaded area). **c)** Depth of corresponding matched events found in USGS catalog, with an inset compares the depth with rise time

Figure 8: Received Levels on all four hydrophones (H32, H38, H40, and H41) for each event of the type: **a)** isolated T-phases, **b)** composite PST phases, **c)** composite PT phases, **d)** paired T-phases, **e)** impulsive I, **f)** impulsive II, **g)** doublet, and **h)** uncategorized phases.

Figure 9: Comparison of local magnitude (M_L) and received levels for the matched events from USGS and hydroacoustic catalog for **a)** impulsive I, **b)** impulsive II, **c)** doublet, and **d)** uncategorized events. The depth variations are shown by different sizes of symbols.